

Autobifunctional Mechanism of Jagged Pt Nanowires for Hydrogen Evolution Kinetics via End-to-End Simulation

Geun Ho Gu, Juhyung Lim, Chengzhang Wan, Tao Cheng, Heting Pu, Sungwon Kim, Juhwan Noh, Changhyeok Choi, Juhwan Kim, William A. Goddard, III,* Xiangfeng Duan,* and Yousung Jung*



Cite This: <https://doi.org/10.1021/jacs.0c11261>



Read Online

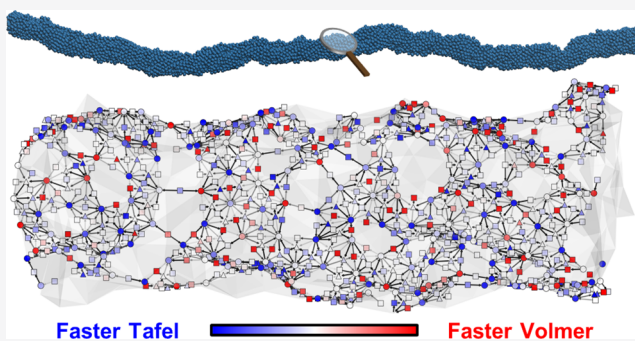
ACCESS |

Metrics & More

Article Recommendations

Supporting Information

ABSTRACT: The extraordinary mass activity of jagged Pt nanowires can substantially improve the economics of the hydrogen evolution reaction (HER). However, it is a great challenge to fully unveil the HER kinetics driven by the jagged Pt nanowires with their multiscale morphology. Herein we present an end-to-end framework that combines experiment, machine learning, and multiscale advances of the past decade to elucidate the HER kinetics catalyzed by jagged Pt nanowires under alkaline conditions. The bifunctional catalysis conventionally refers to the synergistic increase in activity by the combination of two different catalysts. We report that monometals, such as jagged Pt nanowires, can exhibit bifunctional characteristics owing to its complex surface morphology, where one site prefers electrochemical proton adsorption and another is responsible for activation, resulting in a 4-fold increase in the activity. We find that the conventional design guideline that the sites with a 0 eV Gibbs free energy of adsorption are optimal for HER does not hold under alkaline conditions, and rather, an energy between -0.2 and 0.0 eV is shown to be optimal. At the reaction temperatures, the high activity arises from low-coordination-number (≤ 7) Pt atoms exposed by the jagged surface. Our current demonstration raises an emerging prospect to understand highly complex kinetic phenomena on the nanoscale in full by implementing end-to-end multiscale strategies.



Faster Tafel Faster Volmer

INTRODUCTION

Deploying renewable hydrogen as a fuel promises a low-carbon economy, as it burns cleanly (no CO_2 production) to provide a source for nighttime electricity.¹ Yet, the current industrial production chain for hydrogen involves energy-intensive natural gas reforming. It is essential to develop economical, sustainable processes such as water-splitting electrolysis to steer the market toward the green energy future.² Presently, commercial electrolysis cells use Pt-based catalysts for the hydrogen evolution reaction (HER) due to their high activity and stability,³ but the catalyst cost is a major bottleneck.⁴ One direction toward lowering the fuel cell cost is to dramatically reduce the amount of Pt used while maintaining high activity through morphology control,^{5,6} along with other strategies such as Pt alloys⁷ and interfacial interaction engineering.⁸ Here, we focus on HER optimization via morphology control.

Generally, three reactions are known to be involved in the HER (see also the bottom left corner in Figure 1):

- Volmer reaction ($\text{H}^+ + \text{e}^- + * \rightarrow \text{H}^*$, $\text{H}_2\text{O} + \text{e}^- + * \rightarrow \text{H}^* + \text{OH}^-$; * is a site)
- Heyrovsky reaction ($\text{H}^+ + \text{e}^- + \text{H}^* \rightarrow \text{H}_2 + *$, $\text{H}_2\text{O} + \text{e}^- + \text{H}^* \rightarrow \text{H}_2 + *\text{OH}^-$)
- Tafel reaction ($\text{H}^* + \text{H}^* \rightarrow \text{H}_2 + 2*$)

Under acidic conditions, the Volmer reaction that proceeds via proton transfer from hydronium is accepted to be a fast reaction due to an abundance of protons in solution, while the Heyrovsky and Tafel reactions compete for H_2 formation.^{9,10} For alkaline conditions, which are technologically attractive due to the development of anion exchange membranes and non-precious-metal oxygen evolution reaction (OER) catalysts under alkaline conditions, the importance of the HER increases.¹¹ To understand the origin of the slow HER kinetics under alkaline conditions in comparison to acidic conditions, three recent theoretical studies focused on the pH-dependent HER kinetics for the Pt model surface.^{12–14}

Cheng et al. used quantum mechanics molecular dynamics to simulate the water/Pt(100) interface and demonstrated that the hydrogen binding strengthens with increasing pH as the Pt(100) repels water adsorption.¹² Lamoureux et al.

Received: October 26, 2020

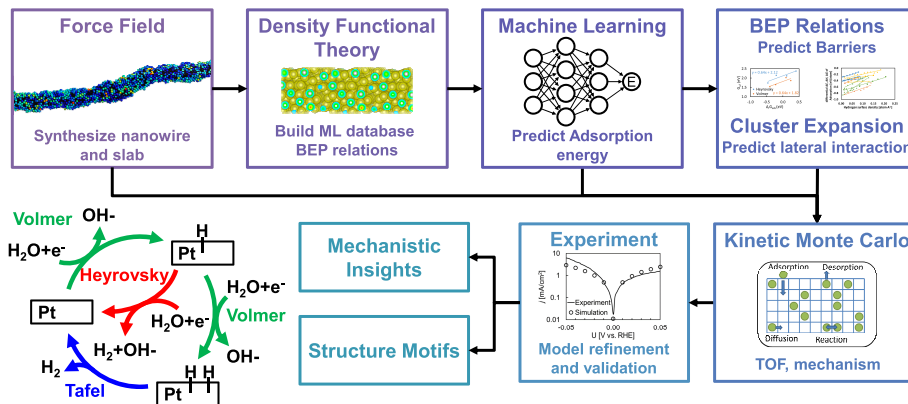


Figure 1. End-to-end workflow for the jagged Pt nanowire simulation. We combine the force field, density functional theory, machine learning, and kinetic modeling to perform a multiscale simulation of the alkaline HER of the jagged Pt nanowires. The model is validated by comparing the simulation result with experimental results, and the mechanism is analyzed. The graphic on the bottom left shows the alkaline HER mechanism involving Volmer, Heyrovsky, and Tafel reactions.

found that the HER on Pt(111) proceeds via the Volmer–Heyrovsky pathway and the proton donor changes from hydronium to water with increasing pH.¹³ An intrinsically greater barrier for proton transfer from water in the Helmholtz plane to the surface is the cause of slower HER kinetics in alkaline media. Liu et al. demonstrated similar conclusions but found that the HER proceeds through Volmer–Tafel.¹⁴

Here, we report an end-to-end simulation of jagged Pt nanowires for HER under alkaline conditions using a machine-learning multiscale strategy¹⁵ with kinetic Monte Carlo (KMC) to reveal novel kinetic insights. This framework yields good agreement with the experimental measurements. We find that both Volmer and Tafel reactions are co-rate-determining steps (RDSs), and notably, the monometallic jagged Pt nanowires offer a bifunctional mechanism: bridge sites are more selective for Volmer, and top and hollow sites are more selective for Tafel, with the two connected via fast diffusion of the adsorbed hydrogen atoms. The optimal hydrogen binding strength for the HER is shown to be lower than zero (irrespective of site type), implying that the conventional design principle for HER to maximize the site activity with a Gibbs free energy of adsorption of H being zero does not hold. The present analysis of surface kinetics reveals that top sites are the most active sites for both Volmer and Tafel reactions, and those with low coordination numbers (≤ 7) are more active. These studies complement the recent report from Chen et al. explaining the extremely high rate for the oxygen reduction reaction (ORR) on jagged Pt nanowires in terms of O² binding and H₂O binding on adjacent sites.¹⁶

RESULTS AND DISCUSSION

Simulated Workflow and Activity Measurement of the Jagged Pt Nanowires. The kinetic simulation was performed using a graph-theoretical KMC simulation.¹⁷ We modeled the alkaline HER system with Volmer, Heyrovsky, Tafel, and diffusion reactions. For the Volmer and Heyrovsky reactions, we considered proton transfer from H₂O (basic) as we performed a simulation at pH of 14.¹⁴ The Section 1 in the Supporting Information describes the derivation of reaction energy and activation energy using a computational hydrogen electrode (CHE) and BEP relations built with the

constant electrode potential (CEP) model. To obtain the adsorption energy on the jagged Pt nanowires, we leveraged the ReaxFF force field and effective medium theory (EMT)^{18,19} to synthesize the jagged Pt nanowires (the structure of which is in close agreement with the experimental characterization^{5,16}) and generate the small jagged Pt slabs (see Section 4 in the Supporting Information) as a model surface of the jagged Pt nanowires.^{5,16} We performed DFT calculations to compute the adsorption energy of 3413 binding sites of the slabs, the local environments of which are extracted¹⁵ and converted to a labeled site representation to train the machine-learning model.²⁰ We tested four models to predict the Gibbs free energy of hydrogen adsorption, $\Delta_r G_{\text{ads}}$: atom-centered symmetric function (ACSF),²¹ crystal graph convolutional neural networks (CGCNN),²² nearest atom distance-Gaussian process (NAD-GP; developed in this work)²³ and SchNet²⁴ (see Section 5 in the Supporting Information). The best model was applied to the jagged Pt nanowires obtained using force field MD simulation.⁵ To account for lateral interaction, we developed and used the cluster expansion model derived from experiments as discussed in Section 6 in the Supporting Information, which sufficiently described the H coverage on Pt surfaces.²⁵ We derived the energetics (see Section 1 in the Supporting Information) and applied BEP relations (see Sections 1 and 3 in the Supporting Information) and performed a KMC simulation to elucidate the mechanisms. The overall framework is illustrated in Figure 1 and demonstrates that the emerging theoretical and machine-learning methods enable the detailed simulation of complex large-scale surfaces.

Validation of the Model. Out of the four different machine learning models we tested for predicting $\Delta_r G_{\text{ads}}$, ACSF showed the lowest out of sample error (0.043 eV mean absolute error); thus, from here on, ACSF is used to predict $\Delta_r G_{\text{ads}}$ (see Figure 2a and Section 5 in the Supporting Information). To quantitatively validate our kinetic simulation, we experimentally synthesized jagged Pt nanowires using the method outlined in refs 5 and 6 and measured the exchange current density, symmetric factor, surface coverage, and Tafel slope (see Section 8 in the Supporting Information for details). To measure exchange current densities, i_0 , the Butler–Volmer equation (−0.05 to 0.05 V vs RHE) and the

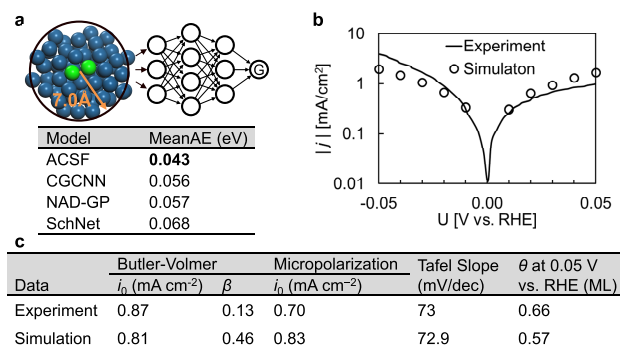


Figure 2. Validation of the machine-learning and the kinetic Monte Carlo model and comparison with the experiment. (a) $\Delta_r G_{\text{ads}}$ prediction machine-learning architecture and the mean absolute error (MeanAE) for the tested models. The local environment ($< 7 \text{ \AA}$) of the binding site atoms (green) is converted to a labeled site representation²⁰ and piped through machine-learning models. We tested atom-centered symmetric function (ACSF),²¹ crystal graph convolutional neural networks (CGCNN),²² nearest atom distance-Gaussian process (NAD-GP; developed in this work),²³ and SchNet,²⁴ and used ACSF for the rest of the article (see Section 5 in the Supporting Information for details). (b) Reaction performed at room temperature with pH 14 and 1 bar of H₂(g) for THE Tafel plot. (c) Simulated exchange current density using Butler–Volmer and micropolarization, coverage (θ), and Tafel slope, being in close agreement with the experiment. β is the symmetric factor.

micropolarization linear equation (-0.01 to 0.01 V vs RHE) were fitted.²⁶ The KMC simulation and experiment were performed at room temperature, pH 14, and 1 bar of H₂(g), and the results are compared in Figure 2. To reproduce the experiment, Tafel barriers and Volmer barriers were adjusted by $+0.06$ and -0.097 eV, respectively (more details are discussed later). The simulated exchange current density (0.81 , and 0.83 mA cm⁻² for Butler–Volmer and linear fitting, respectively) is in good agreement with that measured experimentally (0.87 and 0.70 mA cm⁻², respectively). The coverage (0.57 vs 0.66 monolayers (ML) for simulation and experiment, respectively) and the Tafel slopes (72.9 vs 73 mV/dec for simulation and experiment, respectively) are in close agreement as well. One discrepancy in the symmetric factor (0.45 vs 0.13 for simulation and experiment, respectively) is due to the use of Pt(111) data of ref 9 (0.44) in the model. The use of a more realistic symmetric factor for the Volmer reaction averaged over different binding sites for the jagged nanowires would improve the model. We discuss the uncertainty of our model below.

Hydrogen Evolution Reaction Mechanism. The Gibbs free energy of hydrogen adsorption, $\Delta_r G_{\text{ads}}$, at the zero coverage limit follows a Gaussian shape as shown in Figure 3a. Due to the lateral interaction, $\Delta_r G_{\text{ads}}$ shifts by 0.14 eV with a standard deviation of 0.08 eV. The Tafel and Volmer reactions are co-RDSs, as shown by the degree of rate control analysis²⁷ in Figure 3b in agreement with the previous microkinetic model study on Pt(111).¹⁴ The Heyrovsky reaction is too slow to make any kinetic contribution, but the diffusion process of the adsorbed hydrogen between various surface sites is very fast, at least 3 orders of magnitude faster than either the Tafel or Volmer reactions (turn over frequency of $\sim 10^7$ s⁻¹ of diffusion reactions vs. $\sim 10^1$ s⁻¹ of Tafel and Volmer reactions). Figure 3c shows the average

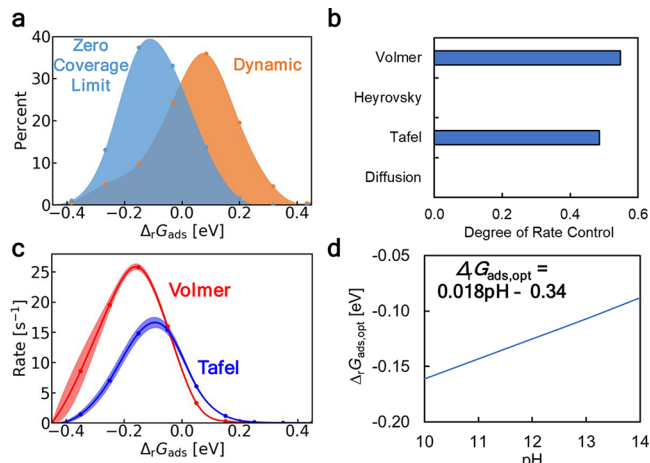


Figure 3. Analysis of kinetics on jagged Pt nanowires at 298 K. (a) Zero coverage limit vs dynamic $\Delta_r G_{\text{ads}}$ calculated at pH 14 and -0.05 V vs RHE. (b) Degree of rate control,²⁷ $d \ln r_i/d(-G_{\text{a},i}^\circ/RT)$ at pH 14 and -0.05 V vs RHE. (c) Average turnover frequency vs $\Delta_r G_{\text{ads}}$ at -0.05 V vs RHE, where the shaded region indicates the 95% confidence interval. (d) Optimal Gibbs free energy of adsorption, $\Delta_r G_{\text{ads},\text{opt}}$ vs the pH at 0 V vs RHE.

turnover frequency of Volmer and Tafel reactions vs the time-averaged Gibbs free energy of adsorption, $\Delta_r G_{\text{ads}}$. Under acidic conditions, the Volmer reaction (H transfer from H₃O⁺) is too fast to be the RDS;^{13,14} thus, the binding site with $\Delta_r G_{\text{ads}} \cong 0$ would be optimal, as it is thermodynamically the most favorable for site occupancy probability and H₂ formation.²⁸ However, under basic conditions, the center of the Volmer (H transfer from H₂O) and Tafel activities for our simulation are at $\Delta_r G_{\text{ads}} = -0.17$ eV and $\Delta_r G_{\text{ads}} = -0.10$ eV, respectively, as shown in Figure 3c. If adsorption and associative desorption reactions are RDSs, the optimal $\Delta_r G_{\text{ads}}$ is observed at a value for which the two reactions have equal activity.²⁹ As the Volmer reaction is faster for $\Delta_r G_{\text{ads}} < 0$, a $\Delta_r G_{\text{ads}}$ value lower than 0 eV is more optimal for the alkaline conditions. This indicates that the design principle (e.g., $\Delta_r G_{\text{ads}}$ -based screening) is not the same for acidic and alkaline conditions. To understand the optimal $\Delta_r G_{\text{ads}}$, we simulated a single-site Pt system using a mean-field microkinetic model and plotted the $\Delta_r G_{\text{ads}}$ values with the highest activity at 0 V vs RHE, $\Delta_r G_{\text{ads},\text{opt}}$, as shown in Figure 3d. The $\Delta_r G_{\text{ads},\text{opt}}$ value is -0.16 eV at pH 10 (where the alkaline Volmer reaction is the adsorption RDS^{13,14}) and increases to -0.09 eV at pH 14.

Autobifunctional Mechanism of Jagged Pt Nanowires. The co-rate-determining steps, the difference in the center of activity with respect to $\Delta_r G_{\text{ads}}$, and the wide $\Delta_r G_{\text{ads}}$ distribution indicate that the jagged Pt nanowires have a bifunctional mechanism. To demonstrate this, we analyzed the microspatial reaction network of the jagged Pt nanowires as shown in Figure 4. The bifunctional catalyst uses a combination of two active sites to overcome two rate-determining steps to improve the overall activity. Conventionally, the two different catalysts are physically mixed or cosynthesized to create the bifunctional catalyst. Here, we find that a monometallic catalyst can exhibit bifunctional characteristics via morphology. For a site with $\Delta_r G_{\text{ads}}$ of 0.0 eV, the Volmer reaction is the RDS with the Gibbs free energy of activation (Figure 4a), $G_{\text{a},\text{f}}$ of 0.68 eV, while for sites with $\Delta_r G_{\text{ads}}$ of -0.12 eV as an example, the Tafel

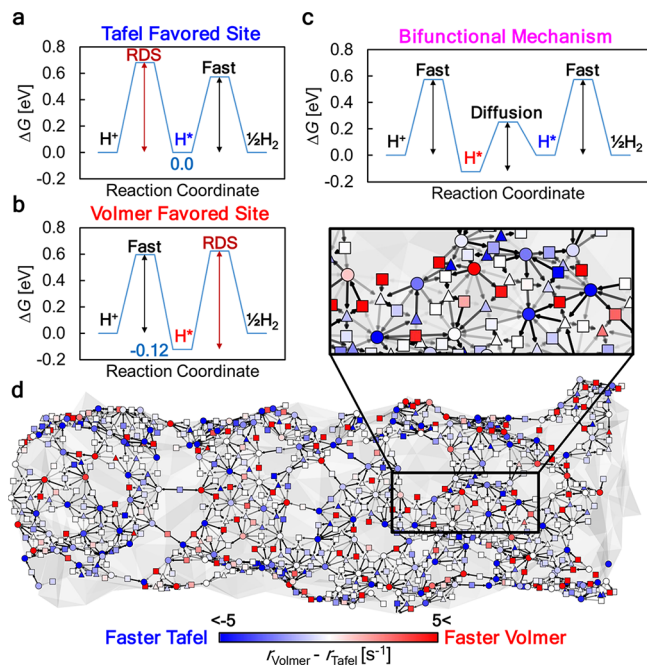


Figure 4. Bifunctional catalysis of the jagged Pt nanowires. (a, b) Hydrogen evolution energetics for $\Delta_r G_{\text{ads}}$ values of (a) 0.0 eV and (b) −0.12 eV. For (a) and (b), Volmer and Tafel reactions are the rate-determining steps (RDS), respectively. (c) Energetics in the top right corner of demonstrating the bifunctional mechanism where the proton can electronically adsorb at a Volmer favorable site and diffuse to a Tafel favorable site to form $\text{H}_2(\text{g})$. (d) Nanowire visualization demonstrating the binding site reaction preference with colored symbols (circles, squares, and triangles are top, bridge, and hollow sites, respectively), where blue and red indicate faster rates in Tafel and Volmer reactions, respectively. We use the range between 5 and −5, as the standard deviation of the activity difference is $\sim 5.11 \text{ s}^{-1}$. The arrows represent the direction of the net flux of hydrogen diffusion, where a darker black indicates a larger net flux. The bifunctional mechanism accounts for a 4-fold increase in activity. The reaction conditions are pH 14, 298 K, and −0.05 V vs RHE.

reaction is the RDS with a $G_{\text{a,f}}$ value of 0.74 eV (Figure 4b). On the jagged Pt nanowires, both of these sites coexist on the surface; hence, a monometallic autobifunctional mechanism is observed where protons electrochemically adsorb on one site (Volmer favored sites) and diffuse to a site with the faster Tafel reaction to form hydrogen (Tafel favored sites).

Figure 4d visualizes the difference in the Volmer and Tafel reaction rates and the diffusion between sites, showing the bifunctional chemistry of the jagged Pt nanowires. The benefit of the bifunctionality can be measured by comparing the current densities with and without hydrogen diffusion. We find that the activity increases by 4-fold (461%) with hydrogen diffusion. To understand the bifunctional effect, we built a microkinetic model with two sites, the $\Delta_r G_{\text{ads}}$ values of which were different from each other. Figure 5 shows the activity gain resulting from coupling the two sites, which demonstrates that the combination of a site with $\Delta_r G_{\text{ads}} > 0$ and a site with $\Delta_r G_{\text{ads}} < 0$ can lead to more than 2 orders of magnitude increase in activity. This bifunctional gain has been hypothetically predicted to occur under certain conditions,³⁰ where we indeed confirm that the bifunctional gain occurs in the jagged Pt nanowires.

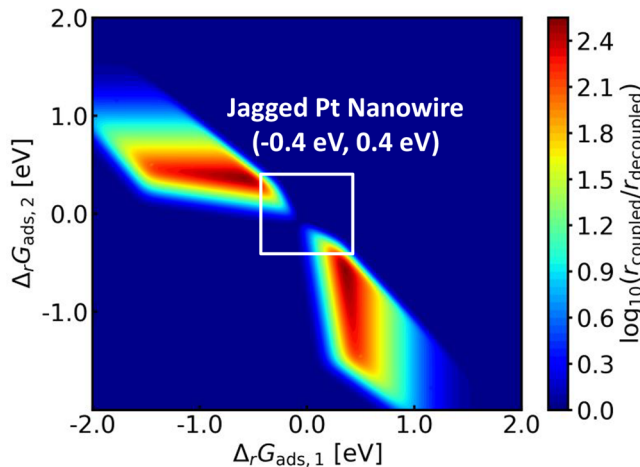


Figure 5. Bifunctional gain in activity with a combination of two sites. A two-site microkinetic model is built where $\Delta_r G_{\text{ads},1}$ and $\Delta_r G_{\text{ads},2}$ are the adsorption energies of the two sites. The color represents the bifunctional gain ratio, where r_{coupled} and $r_{\text{decoupled}}$ are the HER rates when the two sites are coupled and decoupled, respectively. More than 2 orders of magnitude gain in activity can be observed for the combination of two sites with negative and positive adsorption energy. The reaction conditions are pH 14, 298 K, and −0.05 V vs RHE.

Volmer and Tafel Activity by Site Type. We find that the activity is correlated to the binding site type. The activity of the Volmer and Tafel reaction is the highest for the top site, as shown in Figure 6a,c. The top sites behave as the active centers on the jagged Pt nanowires due to the favorable $\Delta_r G_{\text{ads}}$ distribution, as shown in Figure 6d,e. The difference between the site-averaged activity of the Volmer and Tafel reactions shows that Volmer reaction is faster for the bridge sites and the Tafel reaction is faster for the top and hollow sites (Figure 6b). Thus, the top sites consume all of the hydrogen atoms diffused from other top sites, and as the Tafel reaction is faster, top sites also consume other hydrogen atoms diffused from the bridge sites.

Identification of Active Sites. We assessed the correlation between activity and local binding site environment using unsupervised learning methods: smooth overlap of atomic positions (SOAP),³¹ average kernel,³² and t-stochastic neighbor embedding (t-SNE) dimensional reduction analysis.³³ The SOAP and the kernel compute the similarity between the binding sites' environment, and t-SNE reduces the binding site environments into two-dimensional space. Figure 7a plots the two-dimensional representation of binding site environments with $\Delta_r G_{\text{ads}}$ denoted in color. Not surprisingly, we find that the $\Delta_r G_{\text{ads}}$ value is correlated to the coordination number (CN), as shown in Figure S10.³⁴ We plot CN vs $\Delta_r G_{\text{ads}}$ in Figure 7b. For the top site, the correlation between CN and $\Delta_r G_{\text{ads}}$ is obvious, and the sites with $\text{CN} \leq 7$ are more optimal. Synthesizing low-coordinated Pt atoms can further improve the activity. The correlation between CN and $\Delta_r G_{\text{ads}}$ is weak for the bridge site and disappears for the hollow site. To identify structural motifs other than CN, we manually compared structures of optimal and nonoptimal sites, but no apparent trend could be found. Hence, the machine-learning models can understand structural motifs beyond comprehensible motifs. Also, we plot the $\Delta_r G_{\text{ads}}$ values and coordination numbers of top sites of the nanowire segment in Figure 7c to demonstrate that

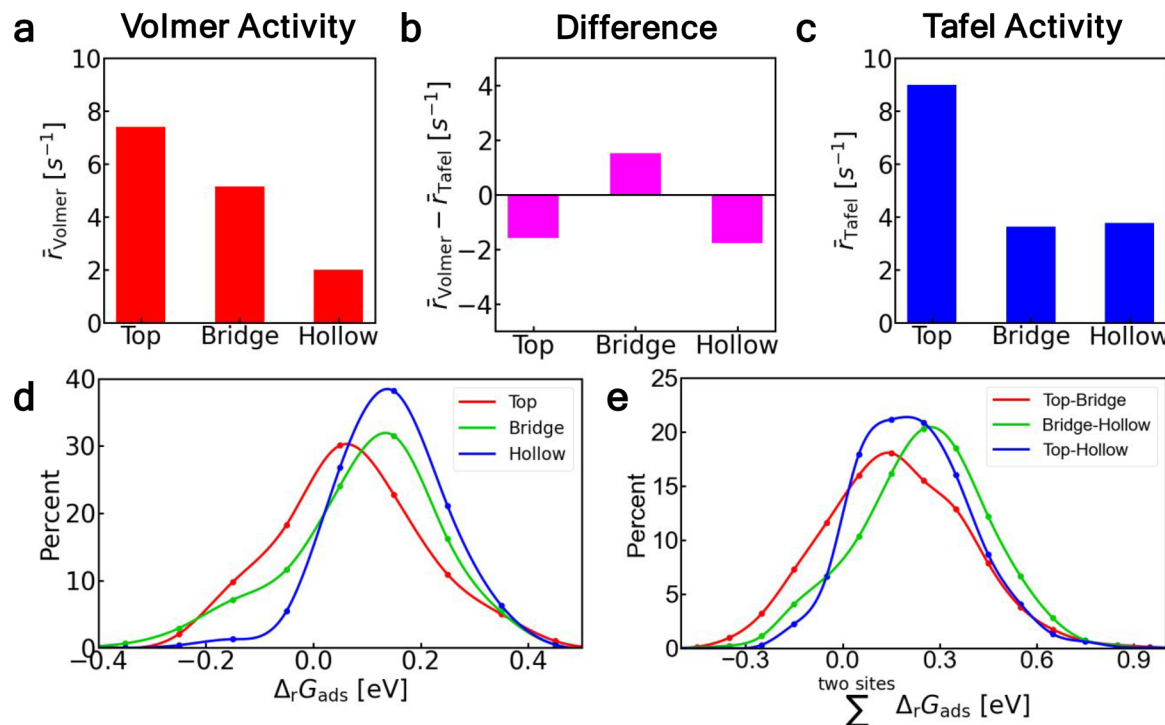


Figure 6. HER activity of the jagged Pt nanowires by the site. Average rates, \bar{r} , of Volmer (**a**), Tafel (**c**), and their difference (**b**) by sites. Distribution of $\Delta_r G_{\text{ads}}$ values of sites (**d**) and the sums of $\Delta_r G_{\text{ads}}$ values of two connected sites (**e**). The top sites are high in both Volmer and Tafel activity. The higher density of the top sites at $\Delta_r G_{\text{ads}} < 0.0$ eV results in higher Volmer activity. For Tafel activity, the optimum occurs at 0.0 eV, as it optimizes the activation energy and the site occupation probability. The top sites have the highest Tafel activity, as top-bridge and top-hollow pairs are dense near $\Delta_r G_{\text{ads}} = 0.0$ eV.

exposed low-coordination sites are closer to the optimal $\Delta_r G_{\text{ads}}$ value.

Limitations of the Model. Due to the multiscale nature of the phenomena and various associated methodologies used here, we address uncertainties of our results and discuss several limitations in this section. As mentioned previously, Tafel barriers and Volmer barriers are adjusted by a constant shifts of +0.06 and -0.097 eV, respectively, in constructing the BEP relation to reproduce the experimental current density as a function of applied potential. The Tafel reaction BEP relations thus obtained also fall within the data points constructed by Skúlason et al.⁹ for Pt(111), Pt(110), and Pt(100) (Figure S7). While the developed Volmer BEP relation does not have a significant uncertainty (see below), only the Pt(111) surface is considered in this study. These constant adjustments are similar to those of the microkinetic model developed on Pt(111),¹⁴ where Volmer barriers were adjusted by -0.07 and -0.03 eV for 0 and 0.83 ML, respectively, and Tafel barriers were adjusted by +0.05 eV for 0.83 ML. Also, the adjustment is within the standard deviation of Tafel and Volmer barriers calculated on Pt(111) using the BEEF-ensemble³⁵ by Lamoureux et al. (0.31 and 0.12 eV, respectively).¹³

We quantify the effect of the important parameters' uncertainty on the reproduced measurements and conclusions. In addition to Volmer and Tafel reactions (Figure 3), the lateral interaction parameter is a sensitive parameter with a degree of rate control of 0.431. Thus, using the 95% confidence interval of Volmer barriers, Tafel barriers, and lateral interaction parameter, the upper and lower bound of the Tafel slope and exchange current density are calculated (Table S3). Overall, the experiment reproducibility is not

significantly affected. The Tafel slope has the highest uncertainty from the Tafel barriers (71.1 to 85.7 mV/dec). While the Volmer reaction has the highest uncertainty in i_0 (0.36 to 1.72 mA cm⁻²), the i_0 value is reproduced within 1 order of magnitude. The uncertainty in the bifunctional gain ratio is the largest with the Tafel barriers (278% to 612%; see Table S3). Overall, the bifunctional mechanism is consistently observed to be well within the uncertainty. We also assess the $\Delta_r G_{\text{ads}}$ distribution vs CN within the uncertainty for the active site identification (Figure S8). The lateral interaction parameter has the highest uncertainty in $\Delta_r G_{\text{ads}}$, but the lower coordinated Pt atoms remain as the active sites.

Our explicit/implicit hybrid DFT calculations have limitations in describing the Pt/water interface, such as the pH-dependent interfacial water structure^{12,36,37} and cation effect.^{38–41} The hydrogen binding strength correlates to the peaks in the underpotential deposition region and has been shown to become stronger with increasing pH on Pt(100).³⁶ The quantum mechanics molecular dynamics study demonstrated that the enhanced binding on Pt(100) is due to the stronger electric potential used under alkaline conditions.¹² Also, the water structure becomes more rigid in a strong electric field, which may slow down the overall HER kinetics.³⁷ Cations form a hydration shell in the Helmholtz plane,^{38,39,41} and the HER activity and activation energy change depending on the cation element.^{38,40} Quantifying these effects computationally for the jagged Pt nanowires is difficult due to the computational cost of the large-scale explicit simulation, but some adjustments made to our model to reproduce the experimental current density may have contributed to implicitly and partially account for these fine effects.

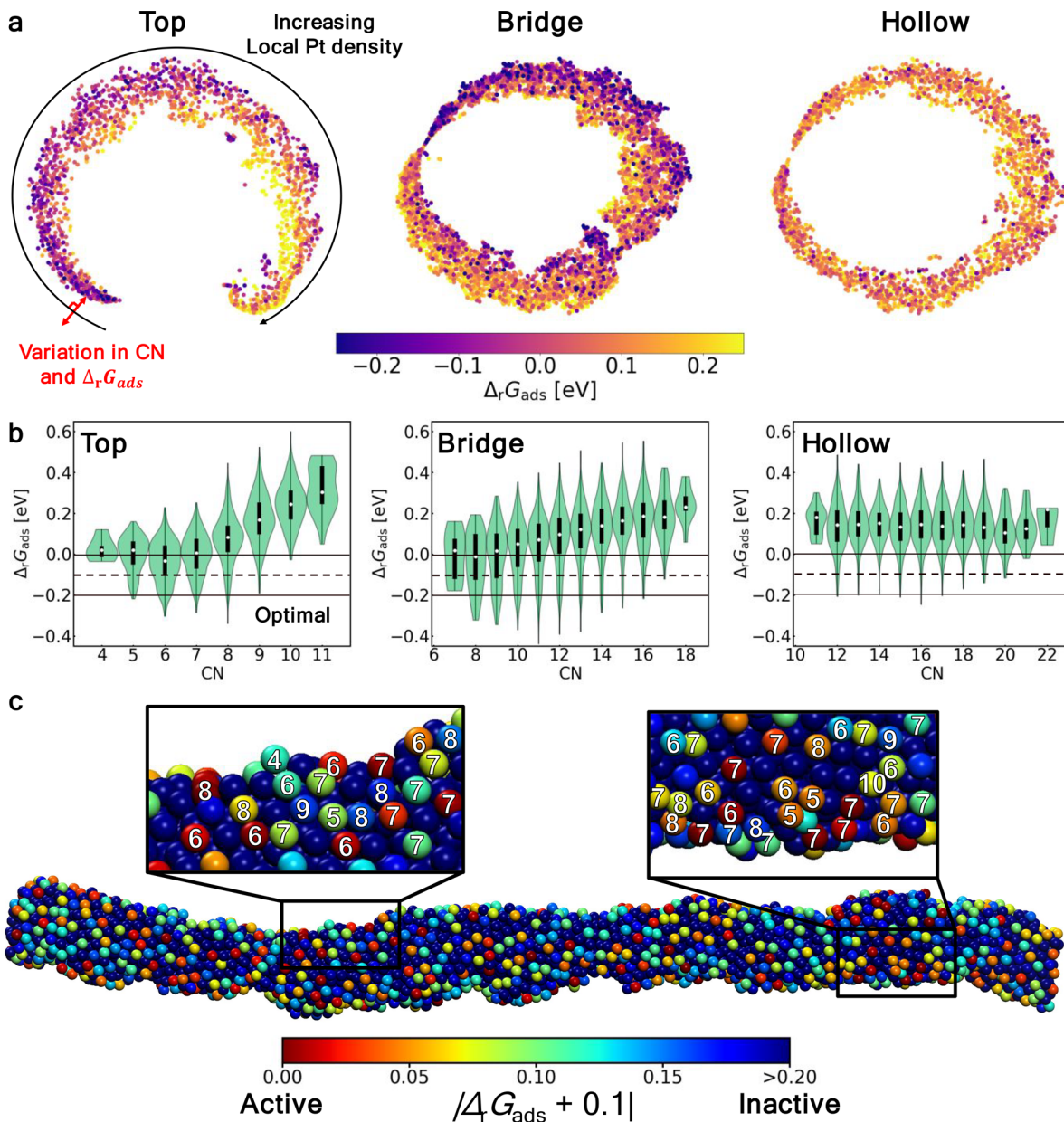


Figure 7. Visualization of the active binding sites. (a) Points and the distance between them representing the site and the dissimilarity between the sites visualized using a SOAP descriptor,³¹ average kernel,³² and t-SNE dimensional reduction analysis.³³ The points are colored by the sites' $\Delta_r G_{ads}$ values for top, bridge, and hollow. As shown in Figure S10, the structural unsupervised learning aligns the site environments on the basis of the local Pt density (number of Pt atoms within 7 Å of the site) along the circular shape, while the direction orthogonal to the circle is correlated with the coordination number. The change in $\Delta_r G_{ads}$ (heat color) is more evident in the orthogonal direction, indicating that the $\Delta_r G_{ads}$ value correlates with the coordination number. (b) Subsequently, the $\Delta_r G_{ads}$ values are plotted against the coordination numbers. (c) A segment of Pt nanowires is visualized where the Pt atoms are colored by the distance from the optimal $\Delta_r G_{ads} \approx -0.1$ eV. The magnification shows that the Pt atoms with low coordination number have more optimal $\Delta_r G_{ads}$ values.

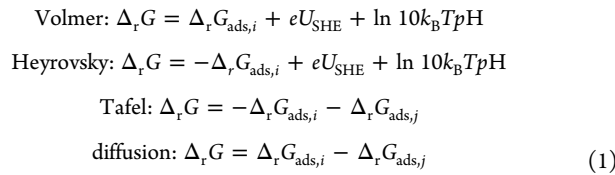
CONCLUSIONS

We demonstrated an end-to-end framework to simulate the kinetics of jagged Pt nanowires with complex morphology using machine learning multiscale strategy, in good agreement with the experimental results under alkaline conditions. As Tafel and Volmer reactions are co-rate-determining steps with distinct BEP relations, we find that the optimal $\Delta_r G_{ads}$ value for the overall rate in alkaline conditions is lower than that under acidic conditions ($\Delta_r G_{ads} < 0$). Due to the co-rate-determining steps and the wide distribution of $\Delta_r G_{ads}$, the jagged Pt nanowires shows an autobifunctional mechanism

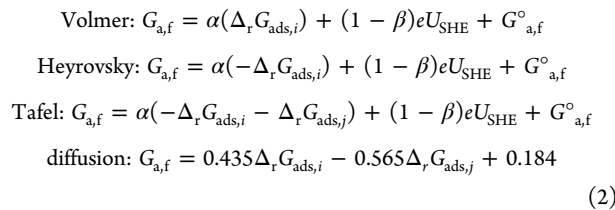
where the stronger binding sites adsorb protons and weaker binding sites activate hydrogen. The top sites are the most active for both Volmer and Tafel reactions, but as the Tafel reaction is faster, top sites also consume hydrogen diffused from bridge sites. Unsupervised learning demonstrates that $\Delta_r G_{ads}$ is correlated to the coordination number, and we find that sites with $CN \leq 7$ are associated with high activity. Beyond the single-metal catalyst, we believe that the demonstrated end-to-end simulation framework has the potential to elucidate the synergistic mechanisms of multi-component alloys and metal–support catalysts and aid in the design of effective catalysts.

METHODS

Energetics. To compute the Gibbs free energy of reaction, $\Delta_r G$, and activation, $G_{a,f}$, we use the computational hydrogen electrode (CHE). $\Delta_r G$ values for the four reactions are



where $\Delta_r G_{\text{ads},i}$ is the Gibbs free energy of H₂ adsorption for site i , U_{SHE} is the electrode potential referenced from the standard hydrogen electrode, k_B is the Boltzmann constant, and T is the temperature. For the Tafel reaction, i and j indicate the two sites undergoing the hydrogen coupling, and for a diffusion reaction, hydrogen is diffusing from site j to i . $G_{a,f}$ values are computed by



where α is the slope of for the dependence of $G_{a,f}$ on coverage, β is the symmetric factor, $G^{\circ}_{a,f}$ is the $G_{a,f}$ value at $\Delta_r G_{\text{ads}} = U_{\text{SHE}} = \text{pH} = 0$. We used the parameters from the literature when available. Otherwise, we used DFT with the CEP method⁴² to parametrize them. The derivation of these equations, the source of parameters, and the computation of the constants are discussed in Section 1 in the Supporting Information. The DFT calculation details and the DFT calculations of missing parameters are discussed in Sections 2 and 3 in the Supporting Information, respectively.

Adsorption Energy Calculation Using Machine Learning. We computed the adsorption energy of hydrogen using a machine learning model. To train our model, we used DFT to compute 3413 adsorption energies of various sites on jagged Pt slabs made using ReaxFF (see Section 4 in the Supporting Information). We used an atom-centered symmetric function²¹ to compute the binding energy as it performed the best out of several models we tested. We used the labeled site representation and ensemble method discussed in our previous work.²⁰ To identify binding sites on jagged Pt nanowires, we used the alpha shape algorithm, which yields a surface area close to those obtained with a cyclic voltammetry curve.^{5,20} The details of the alpha shape algorithm, model cross-validation, and implementation are discussed in Section 5 in the Supporting Information.

Coverage Effect. We derived a cluster expansion model to calculate differential adsorption energy with respect to the coverage from 11 experimental data of Pt(111), Pt(100), and Pt(100). We find that the change in differential adsorption energy is fairly constant with respect to the spatial hydrogen surface density. We exploited this to increase the energy of the system during KMC simulation by 0.098 eV, for every pair of hydrogens within 2.78 Å. The details of the derivation are discussed in Section 6 in the Supporting Information.

Kinetic Monte Carlo Simulation. We implemented the graph-theoretical kinetic Monte Carlo algorithm as outlined by Stamatakis et al.¹⁷ and implemented the reaction constant scaling presented by Núñez et al.⁴³ to speed up the simulation. The detailed pseudocode is provided in Section 7 in the Supporting Information. The Volmer and Tafel rates of a site i are calculated by

$$\begin{aligned} r_{\text{Volmer},i} &= \frac{N_{\text{Volmer},i}}{t} \\ r_{\text{Tafel},i} &= \frac{1}{t} \sum_j \frac{N_{\text{Tafel},i,j}}{2} \end{aligned} \quad (3)$$

where t is the total KMC simulation time, $N_{\text{Volmer},i}$ is the number of Volmer reactions occurring involving site i , and $N_{\text{Tafel},i,j}$ is the number of Tafel reactions occurring from sites i and j .

Experiment. The experimental details are discussed in Section 8 in the Supporting Information.

ASSOCIATED CONTENT

Supporting Information

The Supporting Information is available free of charge at <https://pubs.acs.org/doi/10.1021/jacs.0c11261>.

Derivation of the Gibbs free energies of reaction and activation, DFT calculation details, BEP relation development, ReaxFF MD simulation procedure, machine-learning model development, lateral interaction model development, kinetic Monte Carlo method, experimental procedures, and additional figures and tables (PDF)

AUTHOR INFORMATION

Corresponding Authors

William A. Goddard, III – Materials and Process Simulation Center, California Institute of Technology, Pasadena, California 91125, United States; Email: wag@caltech.edu

Xiangfeng Duan – Department of Chemistry and Biochemistry, California NanoSystems Institute, University of California, Los Angeles, California 90095-1569, United States;  orcid.org/0000-0002-4321-6288; Email: xduan@chem.ucla.edu

Yousung Jung – Department of Chemical and Biomolecular Engineering, Korea Advanced Institute of Science and Technology (KAIST), Daejeon 34141, South Korea;  orcid.org/0000-0003-2615-8394; Email: ysjn@kaist.ac.kr

Authors

Geun Ho Gu – Department of Chemical and Biomolecular Engineering, Korea Advanced Institute of Science and Technology (KAIST), Daejeon 34141, South Korea

Juhyoung Lim – Department of Chemical and Biomolecular Engineering, Korea Advanced Institute of Science and Technology (KAIST), Daejeon 34141, South Korea

Chengzhang Wan – Department of Chemistry and Biochemistry, California NanoSystems Institute, University of California, Los Angeles, California 90095-1569, United States

Tao Cheng – Institute of Functional Nano & Soft Materials, Soochow University Dushu-Lake Campus, Suzhou, Jiangsu 215123, People's Republic of China;  orcid.org/0000-0003-4830-177X

Heting Pu – Department of Chemistry and Biochemistry, California NanoSystems Institute, University of California, Los Angeles, California 90095-1569, United States

Sungwon Kim – Department of Chemical and Biomolecular Engineering, Korea Advanced Institute of Science and Technology (KAIST), Daejeon 34141, South Korea

Juhwan Noh — Department of Chemical and Biomolecular Engineering, Korea Advanced Institute of Science and Technology (KAIST), Daejeon 34141, South Korea

Changhyeok Choi — Department of Chemical and Biomolecular Engineering, Korea Advanced Institute of Science and Technology (KAIST), Daejeon 34141, South Korea

Juhwan Kim — Department of Chemical and Biomolecular Engineering, Korea Advanced Institute of Science and Technology (KAIST), Daejeon 34141, South Korea

Complete contact information is available at:

<https://pubs.acs.org/10.1021/jacs.0c11261>

Notes

The authors declare no competing financial interest.

ACKNOWLEDGMENTS

G.G. is grateful to Dr. Marcel P. Núñez for the useful discussion of the kinetic Monte Carlo simulation. Y.J. acknowledges financial support from the National Research Foundation of Korea (NRF-2017R1A2B3010176 and NRF-2020M3E6A1044370). X.D. gratefully acknowledges support from the National Science Foundation under grant no. NSF 1800580. W.A.G. thanks ONR (N00014-18-1-2155) and NSF (CBET-2005250) for support. T.C. acknowledges financial support from the National Natural Science Foundation of China (Grant No. 2190030094) and the Natural Science Foundation of Jiangsu Province (Grant No. SBK20190810). All data used to generate the results in this paper can be found at https://github.com/kaist-amsg/JPtNW_Manuscript2021. The repository includes the binding energy data for training machine-learning models, ACSF model parameters, and the structures of CEP DFT calculations.

REFERENCES

- (1) Stringer, J.; Horton, L.; Singer, M.; Ahearne, J.; Crabtree, G.; Baker, C.; DeJonghe, L.; Herbst, J.; Dresselhaus, M.; Smalley, R.; Stoller, R. *Basic Research Needs To Assure A Secure Energy Future: A Report from the Basic Energy Science Advisory Committee, Oak Ridge National Laboratory; U.S. Department of Energy*: 2003.
- (2) Miller, E.; Ainscough, C.; Talapatra, A. *Hydrogen Production Status 2006–2013; U.S. Department of Energy*: 2014; Hydrogen and Fuel Cells Program Record.
- (3) Vesborg, P. C. K.; Seger, B.; Chorkendorff, I. Recent Development in Hydrogen Evolution Reaction Catalysts and Their Practical Implementation. *J. Phys. Chem. Lett.* **2015**, *6*, 951.
- (4) Schmidt, O.; Gambhir, A.; Staffell, I.; Hawkes, A.; Nelson, J.; Few, S. Future cost and performance of water electrolysis: An expert elicitation study. *Int. J. Hydrogen Energy* **2017**, *42*, 30470.
- (5) Li, M.; Zhao, Z.; Cheng, T.; Fortunelli, A.; Chen, C.-Y.; Yu, R.; Zhang, Q.; Gu, L.; Merinov, B. V.; Lin, Z.; Zhu, E.; Yu, T.; Jia, Q.; Guo, J.; Zhang, L.; Goddard, W. A.; Huang, Y.; Duan, X. Ultrafine jagged platinum nanowires enable ultrahigh mass activity for the oxygen reduction reaction. *Science* **2016**, *354*, 1414.
- (6) Li, M.; Duanmu, K.; Wan, C.; Cheng, T.; Zhang, L.; Dai, S.; Chen, W.; Zhao, Z.; Li, P.; Fei, H.; Zhu, Y.; Yu, R.; Luo, J.; Zang, K.; Lin, Z.; Ding, M.; Huang, J.; Sun, H.; Guo, J.; Pan, X.; Goddard, W. A.; Sautet, P.; Huang, Y.; Duan, X. Single-atom tailoring of platinum nanocatalysts for high-performance multifunctional electrocatalysis. *Nat. Catal.* **2019**, *2*, 495.
- (7) Greeley, J.; Jaramillo, T. F.; Bonde, J.; Chorkendorff, I.; Nørskov, J. K. Computational high-throughput screening of electrocatalytic materials for hydrogen evolution. *Nat. Mater.* **2006**, *5*, 909.
- (8) Dubouis, N.; Grimaud, A. The hydrogen evolution reaction: from material to interfacial descriptors. *Chem. Sci.* **2019**, *10*, 9165.
- (9) Skúlason, E.; Tripkovic, V.; Björketun, M. E.; Gudmundsdóttir, S.; Karlberg, G.; Rossmeisl, J.; Bligaard, T.; Jónsson, H.; Nørskov, J. K. Modeling the Electrochemical Hydrogen Oxidation and Evolution Reactions on the Basis of Density Functional Theory Calculations. *J. Phys. Chem. C* **2010**, *114*, 18182.
- (10) Fang, Y.-H.; Wei, G.-F.; Liu, Z.-P. Catalytic Role of Minority Species and Minority Sites for Electrochemical Hydrogen Evolution on Metals: Surface Charging, Coverage, and Tafel Kinetics. *J. Phys. Chem. C* **2013**, *117*, 7669.
- (11) Zheng, Y.; Jiao, Y.; Vasileff, A.; Qiao, S.-Z. The Hydrogen Evolution Reaction in Alkaline Solution: From Theory, Single Crystal Models, to Practical Electrocatalysts. *Angew. Chem., Int. Ed.* **2018**, *57*, 7568.
- (12) Cheng, T.; Wang, L.; Merinov, B. V.; Goddard, W. A. Explanation of Dramatic pH-Dependence of Hydrogen Binding on Noble Metal Electrode: Greatly Weakened Water Adsorption at High pH. *J. Am. Chem. Soc.* **2018**, *140*, 7787.
- (13) Lamoureux, P. S.; Singh, A. R.; Chan, K. pH Effects on Hydrogen Evolution and Oxidation over Pt(111): Insights from First-Principles. *ACS Catal.* **2019**, *9*, 6194.
- (14) Liu, L.; Liu, Y.; Liu, C. Enhancing the Understanding of Hydrogen Evolution and Oxidation Reactions on Pt(111) through Ab Initio Simulation of Electrode/Electrolyte Kinetics. *J. Am. Chem. Soc.* **2020**, *142*, 4985.
- (15) Chen, Y.; Huang, Y.; Cheng, T.; Goddard, W. A. Identifying Active Sites for CO₂ Reduction on Dealloyed Gold Surfaces by Combining Machine Learning with Multiscale Simulations. *J. Am. Chem. Soc.* **2019**, *141*, 11651.
- (16) Chen, Y.; Cheng, T.; Goddard, W. A. III Atomistic Explanation of the Dramatically Improved Oxygen Reduction Reaction of Jagged Platinum Nanowires, 50 Times Better than Pt. *J. Am. Chem. Soc.* **2020**, *142*, 8625.
- (17) Stamatakis, M.; Vlachos, D. G. A graph-theoretical kinetic Monte Carlo framework for on-lattice chemical kinetics. *J. Chem. Phys.* **2011**, *134*, 214115.
- (18) Jacobsen, K. W.; Stoltze, P.; Nørskov, J. K. A semi-empirical effective medium theory for metals and alloys. *Surf. Sci.* **1996**, *366*, 394.
- (19) Senftle, T. P.; Hong, S.; Islam, M. M.; Kyela, S. B.; Zheng, Y.; Shin, Y. K.; Junkermeier, C.; Engel-Herbert, R.; Janik, M. J.; Aktulga, H. M.; Verstraelen, T.; Grama, A.; van Duin, A. C. T. The ReaxFF reactive force-field: development, applications and future directions. *Npj Comput. Mater.* **2016**, *2*, 15011.
- (20) Gu, G. H.; Noh, J.; Kim, S.; Back, S.; Ulissi, Z. W.; Jung, Y. Practical Deep-Learning Representation for Fast Heterogeneous Catalyst Screening. *J. Phys. Chem. Lett.* **2020**, *11*, 3185.
- (21) Behler, J. Atom-centered symmetry functions for constructing high-dimensional neural network potentials. *J. Chem. Phys.* **2011**, *134*, 074106.
- (22) Xie, T.; Grossman, J. C. Crystal Graph Convolutional Neural Networks for an Accurate and Interpretable Prediction of Material Properties. *Phys. Rev. Lett.* **2018**, *120*, 145301.
- (23) Rasmussen, C. E. In *Advanced Lectures on Machine Learning: ML Summer Schools 2003, Canberra, Australia, February 2–14, 2003, Tübingen, Germany, August 4–16, 2003, Revised Lectures*; Bousquet, O., von Luxburg, U., Rätsch, G., Eds.; Springer Berlin Heidelberg: Berlin, Heidelberg, 2004; p 63.
- (24) Schütt, K. T.; Sauceda, H. E.; Kindermans, P. J.; Tkatchenko, A.; Müller, K. R. SchNet – A deep learning architecture for molecules and materials. *J. Chem. Phys.* **2018**, *148*, 241722.
- (25) Karlberg, G. S.; Jaramillo, T. F.; Skúlason, E.; Rossmeisl, J.; Bligaard, T.; Nørskov, J. K. Cyclic Voltammograms for H on Pt(111) and Pt(100) from First Principles. *Phys. Rev. Lett.* **2007**, *99*, 126101.
- (26) Lu, S.; Zhuang, Z. Investigating the Influences of the Adsorbed Species on Catalytic Activity for Hydrogen Oxidation Reaction in Alkaline Electrolyte. *J. Am. Chem. Soc.* **2017**, *139*, 5156.

- (27) Campbell, C. T. The Degree of Rate Control: A Powerful Tool for Catalysis Research. *ACS Catal.* **2017**, *7*, 2770.
- (28) Nørskov, J. K.; Bligaard, T.; Logadottir, A.; Kitchin, J. R.; Chen, J. G.; Pandelov, S.; Stimming, U. Trends in the Exchange Current for Hydrogen Evolution. *J. Electrochem. Soc.* **2005**, *152*, J23.
- (29) Andersen, M.; Medford, A. J.; Nørskov, J. K.; Reuter, K. Scaling-Relation-Based Analysis of Bifunctional Catalysis: The Case for Homogeneous Bimetallic Alloys. *ACS Catal.* **2017**, *7*, 3960.
- (30) Andersen, M.; Medford, A. J.; Nørskov, J. K.; Reuter, K. Analyzing the Case for Bifunctional Catalysis. *Angew. Chem., Int. Ed.* **2016**, *55*, 5210.
- (31) Bartók, A. P.; Kondor, R.; Csányi, G. On representing chemical environments. *Phys. Rev. B: Condens. Matter Mater. Phys.* **2013**, *87*, 184115.
- (32) Himanen, L.; Jäger, M. O. J.; Morooka, E. V.; Federici Canova, F.; Ranawat, Y. S.; Gao, D. Z.; Rinke, P.; Foster, A. S. DScribe: Library of descriptors for machine learning in materials science. *Comput. Phys. Commun.* **2020**, *247*, 106949.
- (33) van der Maaten, L.; Hinton, G. Visualizing Data using t-SNE. *Journal of Machine Learning Research* **2008**, *9*, 2579.
- (34) Calle-Vallejo, F.; Loffreda, D.; Koper, M. T. M.; Sautet, P. Introducing structural sensitivity into adsorption–energy scaling relations by means of coordination numbers. *Nat. Chem.* **2015**, *7*, 403.
- (35) Studt, F.; Abild-Pedersen, F.; Varley, J. B.; Nørskov, J. K. CO and CO₂ Hydrogenation to Methanol Calculated Using the BEEF-vdW Functional. *Catal. Lett.* **2013**, *143*, 71.
- (36) Sheng, W.; Zhuang, Z.; Gao, M.; Zheng, J.; Chen, J. G.; Yan, Y. Correlating hydrogen oxidation and evolution activity on platinum at different pH with measured hydrogen binding energy. *Nat. Commun.* **2015**, *6*, 5848.
- (37) Ledezma-Yanez, I.; Wallace, W. D. Z.; Sebastián-Pascual, P.; Climent, V.; Feliu, J. M.; Koper, M. T. M. Interfacial water reorganization as a pH-dependent descriptor of the hydrogen evolution rate on platinum electrodes. *Nature Energy* **2017**, *2*, 17031.
- (38) Liu, E.; Li, J.; Jiao, L.; Doan, H. T. T.; Liu, Z.; Zhao, Z.; Huang, Y.; Abraham, K. M.; Mukerjee, S.; Jia, Q. Unifying the Hydrogen Evolution and Oxidation Reactions Kinetics in Base by Identifying the Catalytic Roles of Hydroxyl-Water-Cation Adducts. *J. Am. Chem. Soc.* **2019**, *141*, 3232.
- (39) Jiao, L.; Liu, E.; Mukerjee, S.; Jia, Q. In Situ Identification of Non-Specific Adsorption of Alkali Metal Cations on Pt Surfaces and Their Catalytic Roles in Alkaline Solutions. *ACS Catal.* **2020**, *10*, 11099.
- (40) Weber, D. J.; Janssen, M.; Oezaslan, M. Effect of Monovalent Cations on the HOR/HER Activity for Pt in Alkaline Environment. *J. Electrochem. Soc.* **2019**, *166*, F66.
- (41) Strmcnik, D.; Kodama, K.; van der Vliet, D.; Greeley, J.; Stamenkovic, V. R.; Marković, N. M. The role of non-covalent interactions in electrocatalytic fuel-cell reactions on platinum. *Nat. Chem.* **2009**, *1*, 466.
- (42) Van den Bossche, M.; Skúlason, E.; Rose-Petrucci, C.; Jónsson, H. Assessment of Constant-Potential Implicit Solvation Calculations of Electrochemical Energy Barriers for H₂ Evolution on Pt. *J. Phys. Chem. C* **2019**, *123*, 4116.
- (43) Núñez, M.; Robie, T.; Vlachos, D. G. Acceleration and sensitivity analysis of lattice kinetic Monte Carlo simulations using parallel processing and rate constant rescaling. *J. Chem. Phys.* **2017**, *147*, 164103.